

Dichroic Mirror Pulses for Optimized Higher-Order Atomic Bragg Diffraction

D. Pfeiffer^{1,*}, M. Dietrich^{1,†}, P. Schach^{1,‡}, G. Birkl^{1,2,‡} and E. Giese^{1,†}

¹Technische Universität Darmstadt, Fachbereich Physik, Institut für Angewandte Physik, Schlossgartenstraße 7, 64289 Darmstadt, Germany

²Helmholtz Forschungsakademie Hessen für FAIR (HFHF), Campus Darmstadt, Schlossgartenstraße 2, 64289 Darmstadt, Germany

Increasing the sensitivity of light-pulse atom interferometers progressively relies on large-momentum transfer techniques. Precise control of such methods is imperative to exploit the full capabilities of these quantum sensors. One key element is the mitigation of deleterious effects such as parasitic paths deteriorating the interferometric signal. In this Letter, we present the experimental realization of dichroic mirror pulses for atom interferometry, its scalability to higher-order Bragg diffraction, and its robustness against initial momentum spread. Our approach selectively reflects resonant atom paths into the detected interferometer output, ensuring that these contribute to the signal with intent. Simultaneously, parasitic paths are efficiently transmitted by the mirror and not directed to the relevant interferometer outputs. This method effectively isolates the desired interferometric signal from noise induced by unwanted paths. It can be readily applied to existing setups capable of higher-order Bragg diffraction.

This article has been published in *Physical Review Research* 7, L012028 (2025) under the terms of the Creative Commons Attribution License 4.0 [CC BY]. DOI: <https://doi.org/10.1103/PhysRevResearch.7.L012028>

Large momentum transfer (LMT) [1, 2] is one promising approach for scaling the sensitivity of light-pulse atom interferometers. By complementing architectures based on extending free-fall times in microgravity [3–6], large-scale fountain setups [7–10], and relaunch geometries [11–15], LMT promotes atom interferometers to high-precision quantum sensors. Among other achievements, it has facilitated the most precise determination of the fine-structure constant [16, 17], the generation of record-scale spatial superpositions [10], and competitive tests of relativity [18]. While today’s technology enables momentum transfer of hundreds of photon recoils [16, 17, 19–21], proposals for atom-interferometric gravitational-wave or dark-matter detection [8, 22, 23] rely on a transfer exceeding 10^2 to 10^4 photon recoils and thus on optimizing LMT. Among the most prominent LMT techniques are (i) Bloch oscillations [24–28], (ii) sequential pulses [29–31], (iii) double diffraction [32–34], and (iv) higher-order diffraction [23, 35–37] with many experiments combining several techniques [14, 16, 17, 37–39].

Although each method has its own characteristics, all are susceptible to imperfect momentum transfer and pulse infidelity [40], so parasitic momenta are populated inherently. These imply overall loss, diffraction phases [41, 42], and introduce unintended paths to the interferometer. These paths are redirected into the detected output ports of the interferometer, causing multipath interference [43–46] deteriorating the sensitivity. Current mitigation techniques include (i) tailored design of pulse shapes to suppress the population of parasitic momenta [47, 48], sometimes leveraged by optimal control [40, 49–53] and applied to the full pulse sequence [54], (ii) optimal-control techniques to enhance the signal of multipath interference [55], or (iii) exploitation of destructive interference of parasitic paths [56].

We present a demonstration of a complementing technique optimizing the mirror pulses of the interferometer. Our approach has been inspired by a proposal [57, 58] of momentum-selective, i. e., dichroic mirror pulses (DMP) based on Bragg diffraction [59, 60] that only redirect the two intentionally populated, i. e., resonant paths (distinguishable through their

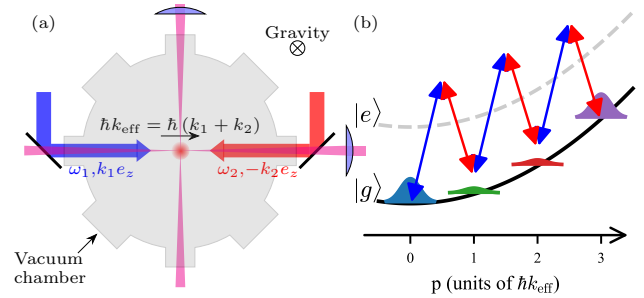


FIG. 1. Experimental setup and energy band structure of higher-order Bragg diffraction. (a) An atom ensemble with narrow momentum distribution is prepared via Bose-Einstein condensation in a crossed dipole trap (transparent red). Two counterpropagating laser beams (blue and red) induce Bragg diffraction and transfer momenta $\hbar k_{\text{eff}}$ as beam splitters and mirrors. (b) Energy-momentum conservation in a third-order Bragg process. Blue and red arrows denote the induced absorption and emission of photons of the corresponding Bragg beams. The light is strongly detuned with respect to one-photon transitions.

momenta), while being made transparent for the dominant parasitic paths, which are not redirected to the detected output of the interferometer. Such an evolution is induced by applying a pulse area of π to the resonant paths, while parasitic orders experience pulse areas of multiples of 2π . We establish the scalability of this technique through an examination of resonant third- and fifth-order diffraction. Accompanying simulations prove that the method exhibits robust performance across a wide range of momentum spreads instead of being velocity selective. As a consequence, this technique can be readily applied to existing setups capable of higher-order Bragg diffraction.

To induce Bragg diffraction, two counterpropagating laser beams with frequency difference $\Delta\omega = \omega_1 - \omega_2$ couple two momenta via a virtual state, see Fig. 1. Subsequently absorbing a photon from one laser field and re-emitting it into the counterpropagating field transfers momentum $\hbar k_{\text{eff}} = \hbar(k_1 + k_2)$ to the atom as a consequence of momentum conservation, where k_j is

the modulus of the wave vector of field j . For frequencies $\omega_{1,2}$ far detuned from the one-photon transition, Rabi oscillations between the two resonant momenta are induced at a two-photon Rabi frequency Ω_R . Coupling the initial momentum p_0 to higher momentum states is possible by transferring $n\hbar k_{\text{eff}}$ momenta through a $2n$ -photon process [61], resonantly populating the momentum $p_n = p_0 + n\hbar k_{\text{eff}}$. For an atom of mass m , the resonance condition is given by $\Delta\omega = n\hbar k_{\text{eff}}^2/(2m) + p_0 k_{\text{eff}}/m$ [see Fig. 1(b)], where the effective $2n$ -photon Rabi frequency scales with the n th power of Ω_R . In this Letter, we focus on third- and fifth-order Bragg diffraction $n = 3$ and $n = 5$ which demonstrate all relevant mechanisms, especially since the dominating parasitic momenta p_i are inherently given by $i = 1$ and $i = n - 1$ [57, 58].

For the preparation of ultracold ensembles of ^{87}Rb , we produce in a far-detuned crossed optical dipole trap a Bose-Einstein condensate (BEC) of typically 20000 atoms (temperature: 25(5) nK, condensate fraction $\geq 80\%$) by forced evaporative cooling [62]. The ensemble in the atomic ground state $|g\rangle = |5^2S_{1/2}, F = 1\rangle$ is released with momentum $p_0 = 0$ along the direction of the Bragg beams. An expansion time of 3 ms converts the ensemble's mean field energy to kinetic energy, after which the momentum spread of the ensemble (fitted to a Gaussian) is $\Delta p = 0.13(3)\hbar k_{\text{eff}}$. To induce the desired order of diffraction, the frequency difference of a pair of counter-propagating horizontally-aligned laser beams is adjusted to the respective resonance condition $\Delta\omega = n \times 2\pi \times 15.1$ kHz. The detuning $2\pi \times 3.2$ GHz to the state manifold $|e\rangle = |5^2P_{3/2}, F = 2\rangle$ is sufficiently large to suppress its population by one-photon absorption. The waist $w_0 = 1170(50)$ μm of the Bragg beams significantly exceeds the size of the expanded atom cloud (≤ 100 μm) and the distance traveled by the atoms (≤ 250 μm). We apply a pulse with a Blackman window function $f(t) = 0.42 - 0.5 \cos(2\pi t/\tau) + 0.08 \cos(4\pi t/\tau)$ defined for a duration $0 \leq t \leq \tau$ with FWHM $\approx 0.405\tau$ and $f(\tau/2) = 1$ as smooth pulse envelope. After a Bragg-pulse sequence, a time of flight (TOF) of typically 15 ms projects the final atomic momentum distribution to the far-field and spatially separates different momenta. Detection is performed by resonant-absorption imaging.

Higher-order diffraction requires longer pulses or increased laser power, implying an increased Ω_R . The two parameters are balanced to minimize velocity selectivity while still observing a two-level behavior between resonant momenta. However, this quasi-Bragg regime [43, 59, 63, 64] leads to inevitable population of parasitic orders p_i . By using smooth pulse envelopes (like Blackman pulses) this issue can be mitigated, but not eliminated.

Fixing $\tau = 90$ μs and scanning Ω_R by varying the optical power of the pulse [65] when tuned to third-order resonance $n = 3$, we determine the probability of populating momenta p_i by extracting the atom numbers in the relevant orders $i = 0, 1, 2, 3$ and normalizing to their sum. In Fig. 2(a) we show the probabilities of p_0 (red diamonds) and $p_3 = p_0 + 3\hbar k_{\text{eff}}$ (blue dots) as a function of Ω_R . From this scan we extract Ω_R for beam splitter ($\pi/2$) and mirror (π) pulses for third-order

diffraction. The transfer to momentum p_3 is limited to 65 %, which we attribute to velocity selectivity [66].

Our experimental observations are supported by simulations implementing the effective Hamiltonian [63]

$$\hat{H} = \frac{\hat{p}^2}{2m} + 2\hbar\Omega_R f(t) \cos^2\left(\frac{k_{\text{eff}}\hat{x} - \Delta\omega t + \phi}{2}\right), \quad (1)$$

with the phase of the Bragg beams ϕ and $[\hat{x}, \hat{p}] = i\hbar$, since atomic interactions can be neglected due to the low atom density after expansion. For these simulations, we use a Split-Step-Fourier method implementing the palindromic *PP 3/4 A scheme* [67]. Since our figure of merit, the diffracted population, is not expected to depend on the laser phase in Bragg diffraction, we choose $\phi = 0$ for our simulations. We fit our numerical model to the data using the experimental values of Ω_R and τ and only leaving the initial spread Δp as a free parameter. The results are shown as solid lines in Fig. 2(a) and agree well with our experiments. Applying the same routine to a larger data set varying $50 \mu\text{s} \leq \tau \leq 150 \mu\text{s}$, we infer $\Delta p = 0.13(1)\hbar k_{\text{eff}}$, matching the experimental value.

Using the parameters obtained from this fit, we extend our simulations to a full Mach-Zehnder ($\pi/2 - \pi - \pi/2$) interferometer (MZI). Besides the resonant paths p_0 and p_3 , parasitic paths emerge after the first beam splitter. To demonstrate their impact, we show in Fig. 2(b) a path-resolved version of the MZI simulation. The atom density is displayed on logarithmic scale with the input to every path normalized to unity. Dashed colored lines indicate the paths of non-displayed orders and dashed black lines the output ports of the MZI associated with p_0 and p_3 . The final section of the time evolution hides the atoms not detected in these ports to augment the contribution of each path to the signal. The resonant paths 0 and 3 suffer loss from velocity selectivity, but the bulk of the population couples into the output ports as intended. Because the mirror pulse also redirects the parasitic paths 1 and 2, they are coupled into the relevant output ports, interfering with resonant paths and corrupting the signal. While the effect is small for adiabatic pulses that suppress the initial population of parasitic paths, it can limit the sensitivity of the interferometer [57]. To verify the numerical observation that the mirror pulse redirects both resonant and parasitic paths, we selectively prepare atoms in four input states $p_{\text{in}} \in \{p_0, p_1, p_2, p_3\}$ by applying Bragg pulses at the respective resonance, as shown in the left column of Fig. 2(c) by absorption images in the far field. After 4 ms of propagation, we apply the third-order mirror pulse ($\tau = 90$ μs , $\Omega_R = 2\pi \times 23(2)$ kHz). The right column of Fig. 2(c) presents the resulting momentum distributions. The resonant orders (purple and blue) are efficiently reflected, but so are the parasitic orders (red and green), which are redirected to the exit ports with high efficiency.

To overcome this problem, we implement a DMP that is reflective only for the resonant paths 0 and 3 while not redirecting the parasitic paths 1 and 2. Similar to the experiment presented in Fig. 2(c), we prepare ensembles in all four relevant p_{in} and apply a mirror pulse resonant to third-order diffraction, varying τ and Ω_R . To obtain the reflectivity $R_{\text{in,out}}$ for each path, we

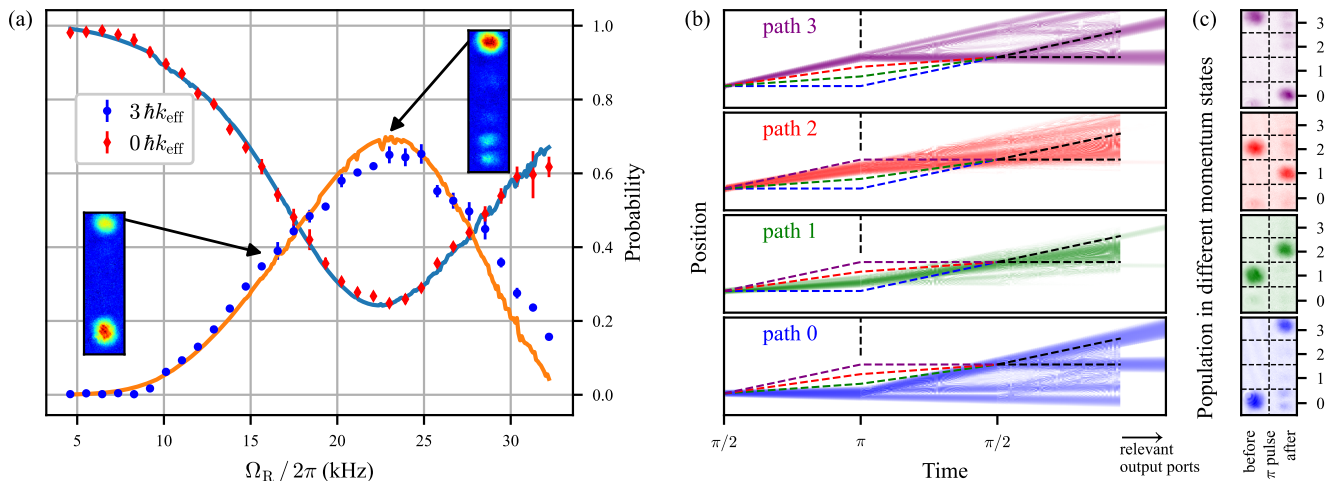


FIG. 2. Experiment and simulation of third-order Bragg diffraction. (a) Resonant Rabi scan for a fixed duration $\tau = 90 \mu\text{s}$ of a Blackman pulse. Scanning Ω_R induces Rabi oscillations between momentum states p_0 and p_3 (measured probabilities as red diamonds and blue dots). Solid lines show a corresponding simulation with a fitted width $\Delta p = 0.13(1)\hbar k_{\text{eff}}$ of a Gaussian momentum distribution. False-color insets depict momentum distributions after a beam splitter (left) and mirror pulse (right) with population in p_0 at the bottom and in p_3 on top. The undeflected density lobes of p_0 are caused by momentum selectivity. (b) The simulated time evolution separated into two resonant (0, 3) and two parasitic (1, 2) paths on a logarithmic color map, with the deleted paths sketched by colored dashed lines. The dashed black lines after the second beam splitter indicate the relevant output ports. In the final section, all population that is not detected in these ports is blanked. The simulation demonstrates that also parasitic orders are reflected and coupled into the output ports. (c) Confirming these numerical findings, we present experimental absorption images of momentum distributions before (left) and after (right) the mirror pulse. The resonant orders (purple and blue) are efficiently reflected, but so are the parasitic orders (red and green), which are redirected to the exit ports with high efficiency.

measure the final probability of all four output momenta p_{out} by integrating over the respective momentum distribution in the far field and normalizing it. In Fig. 3(a) (left column) we show the measured values for $R_{0,3}$ and $R_{1,2}$. Corresponding simulations are depicted in the right column, showing excellent agreement. The white dashed line indicates the Rabi-frequency scan of Fig. 2(a). Since resonant paths are redirected by six-photon processes but parasitic paths by two-photon transitions, their multi-photon Rabi frequencies differ, as can be seen from different oscillation periods in the top and bottom panels. This behavior suggests a parameter set where resonant orders experience a pulse area π , while parasitic orders experience pulse areas of multiples of 2π . In fact, for $\tau = 120 \mu\text{s}$ and $\Omega_R = 2\pi \times 21(2) \text{ kHz}$ we observe a DMP with $R_{0,3} = 0.62(1)$ and $R_{1,2} = 0.08(1)$ (white diamonds). In comparison to the parameters of Fig. 2(a) with $R_{0,3} = 0.65(2)$ and $R_{1,2} = 0.72(1)$ (black crosses), the reflectivity of parasitic paths drops significantly while the one of resonant paths remains almost unaltered. The pronounced reflectivity of resonant paths combined with the low reflectivity of parasitic paths implements the intended DMP.

As in Fig. 2(b), we display a path-resolved MZI simulation in Fig. 3(b). Since the DMP does not redirect parasitic paths, they do not overlap with resonant arms at the second beam splitter and are not coupled into the two relevant output ports. We verify this dichroic behavior experimentally. Figure 3(c) displays the momentum distributions before (left) and after (right) the DMP. Indeed, the DMP is reflective for resonant

paths and redirects them to the exit ports, while maintaining near-perfect transparency for both parasitic paths where the output momentum distribution resembles the input.

While the concept of DMPs has been theoretically studied for momentum eigenstates [57], our experiments demonstrate its applicability to realistic momentum distributions. To analyze its robustness, we numerically determine $R_{0,3}$ and $R_{1,2}$ as a function of the initial momentum spread Δp in Fig. 4(a). For increasing Δp we observe that $R_{0,3}$ deteriorates for both pulse settings and approaches unity for small Δp , as expected from velocity selectivity. However, the DMP exhibits markedly reduced reflectivity $R_{1,2}$ over the full range in Δp . Hence, our simulations highlight that DMPs are operational for a broad range of momentum distributions.

Our results can be transferred to any odd diffraction order, in particular to fifth order, which is a good compromise [66] between available laser power, velocity selectivity, and loss from spontaneous emission. We experimentally demonstrate this scalability by implementing a fifth-order DMP and measuring $R_{0,5}$, $R_{1,4}$, and $R_{2,3}$ [Fig. 5(b)]. The latter two reflectivities are associated with parasitic paths as shown in Fig. 5(a). The different scaling of the multi-photon Rabi frequencies [63] allows to identify parameters [$\tau = 100 \mu\text{s}$, $\Omega_R = 2\pi \times 52(5) \text{ kHz}$] where the pulse area is close to π for the resonant path, but 4π and 6π for the parasitic ones, giving reflectivities $R_{0,5} = 0.57(1)$, $R_{1,4} = 0.16(1)$, $R_{2,3} = 0.10(1)$. In Fig. 4(b) we simulate the influence of Δp on the reflectivities, using $\Omega_R = 2\pi \times 52.9 \text{ kHz}$ which has been obtained from a fit to the Rabi scan of $R_{1,4}$ for

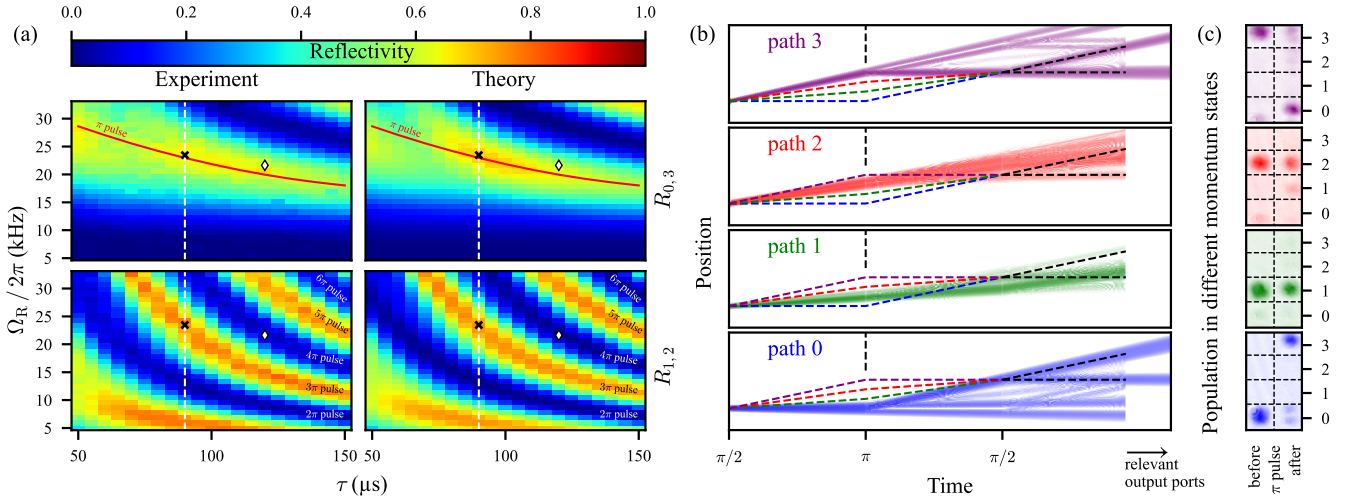


FIG. 3. Experiment and simulation of third-order Bragg diffraction with DMPs. (a) Comparison of experimental (left) and numerical (right) reflectivities $R_{0,3}$ (top) for resonant six-photon and $R_{1,2}$ (bottom) for parasitic two-photon diffraction. Scanning τ and Ω_R reveals different effective Rabi frequencies for both cases. The white diamonds indicate the DMP [$\tau = 120 \mu\text{s}$, $\Omega_R = 2\pi \times 21(2) \text{ kHz}$] with significantly improved performance over the mirror pulse (black cross) obtained in Fig. 2(a). The labels indicate pulse areas of multiples of π . Panels (b) and (c) modify their counterparts of Fig. 2 using the optimum DMP. In (b), resonant paths are reflected efficiently but parasitic paths are fully transmitted by the mirror pulse and thus not coupled into the relevant output ports, as highlighted by the lack of relevant population in the final section of the plot. (c) We confirm this dichroic behavior experimentally by absorption images of the momentum distribution before (left) and after (right) the DMP, where parasitic paths are not reflected by the DMP and almost fully remain in their input momentum class.

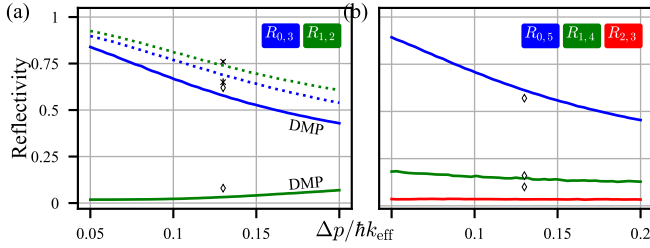


FIG. 4. Simulated reflectivities (lines) as a function of momentum spread Δp complemented by experimental values for $\Delta p = 0.13\hbar k_{\text{eff}}$ (crosses and diamonds). (a) Third-order diffraction: Comparing a pulse with the parameters of maximal $R_{0,3}$ from Fig. 2(a) (dotted lines and black crosses) to the DMP (solid lines and white diamonds), we observe a drastic drop in the reflectivity of parasitic paths for the DMP for all Δp . (b) A DMP of fifth order shows analog behavior.

$\tau = 100 \mu\text{s}$ and lies within the error margin of the experimental value reported above. We again observe drastically reduced parasitic reflectivities for the DMP for all Δp .

Additional simulations for $n = 7$ and $n = 9$ (with $\Delta p = 0.05\hbar k_{\text{eff}}$) demonstrate that high reflectivity of the resonant and simultaneous suppression of the reflectivities for all parasitic orders is achievable, indicating that this technique scales to even higher diffraction orders. Note, that extending the scheme to even diffraction orders has the disadvantage that the central parasitic path will always couple into the output ports, similar to double diffraction [46]. While we have focused on the reflectivity of resonant and parasitic paths in this Letter, it is possible to use different optimization strategies and more

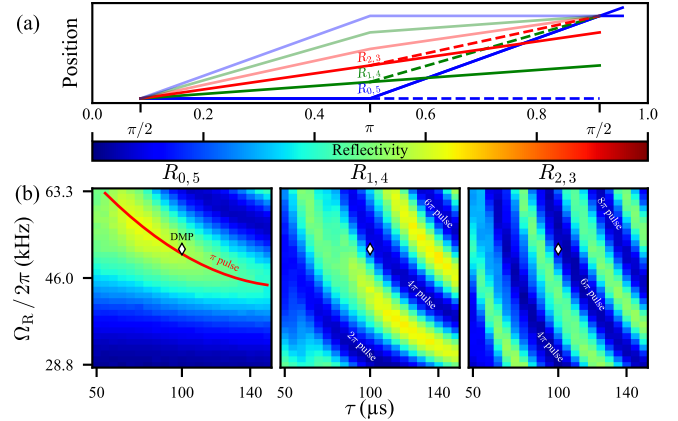


FIG. 5. Fifth-order MZI (a) highlighting the paths associated with the reflectivities $R_{0,5}$, $R_{1,4}$, and $R_{2,3}$ as measured in (b) for different pulse lengths τ and two-photon Rabi frequencies Ω_R . The DMP is marked by a white diamond ($\tau = 100 \mu\text{s}$, $\Omega_R = 2\pi \times 52(5) \text{ kHz}$), where the resonant path experiences a pulse area close to π , while the parasitic paths undergo 4π and 6π pulses, respectively.

refined parameters that, e. g., include the population of parasitic orders after the initial beam splitter or to customize the method to geometries beyond MZIs [68]. After all, the ultimate figure of merit is the sensitivity of a closed interferometer, which intrinsically depends on the contrast. Using optimal control or reinforcement machine learning techniques might improve the performance of DMPs even further [50, 51, 69].

Although we studied DMPs for higher-order Bragg diffrac-

tion, the concept may be transferred to other approaches of LMT like sequential pulses [29–31], which can be also applied to other diffraction, e. g. clock transitions [29, 70]. Since composite pulses often resort to a combination of several LMT techniques, each with its own mitigation scheme for parasitic orders, the interplay of these strategies will eventually be of relevance for advanced experiments [14, 16, 17, 37–39]. Adding DMPs to the toolbox of LMT will foster the implementation of ambitious proposals for high-precision atom interferometry.

We thank L. Lind and the QUANTUS and INTENTAS teams for helpful discussions. The QUANTUS project is supported by the German Space Agency at the German Aerospace Center (Deutsche Raumfahrtagentur im Deutschen Zentrum für Luft- und Raumfahrt, DLR) with funds provided by the Federal Ministry for Economic Affairs and Climate Action (Bundesministerium für Wirtschaft und Klimaschutz, BMWK) due to an enactment of the German Bundestag under Grant No. 50WM2450E (QUANTUS-VI).

* apqpub@physik.tu-darmstadt.de

† <https://www.iap.tu-darmstadt.de/tqo>

‡ <https://www.iap.tu-darmstadt.de/apq>

- [1] J. E. Debs, P. A. Altin, T. H. Barter, D. Döring, G. R. Dennis, G. McDonald, R. P. Anderson, J. D. Close, and N. P. Robins, Cold-atom gravimetry with a Bose-Einstein condensate, *Phys. Rev. A* **84**, 033610 (2011).
- [2] S.-w. Chiow, T. Kovachy, H.-C. Chien, and M. A. Kasevich, 102hk Large Area Atom Interferometers, *Phys. Rev. Lett.* **107**, 130403 (2011).
- [3] H. Müntinga, H. Ahlers, M. Krutzik, A. Wenzlawski, S. Arnold, D. Becker, K. Bongs, H. Dittus, H. Duncker, N. Gaaloul, C. Gherasim, E. Giese, C. Grzeschik, T. W. Hänsch, O. Hellmig, W. Herr, S. Herrmann, E. Kajari, S. Kleinert, C. Lämmerzahl, *et al.*, Interferometry with Bose-Einstein Condensates in Microgravity, *Phys. Rev. Lett.* **110**, 093602 (2013).
- [4] B. Barrett, L. Antoni-Micollier, L. Chichet, B. Battelier, T. Lévêque, A. Landragin, and P. Bouyer, Dual matter-wave inertial sensors in weightlessness, *Nat. Commun.* **7**, 13786 (2016).
- [5] M. D. Lachmann, H. Ahlers, D. Becker, A. N. Dinkelaker, J. Grosse, O. Hellmig, H. Müntinga, V. Schkolnik, S. T. Seidel, T. Wendrich, A. Wenzlawski, B. Carrick, N. Gaaloul, D. Lütke, C. Braxmaier, W. Ertmer, M. Krutzik, C. Lämmerzahl, A. Peters, W. P. Schleich, K. Sengstock, A. Wicht, P. Windpassinger, and E. M. Rasel, Ultracold atom interferometry in space, *Nat. Commun.* **12**, 1317 (2021).
- [6] J. R. Williams, C. A. Sackett, H. Ahlers, D. C. Aveline, P. Boegel, S. Botsi, E. Charron, E. R. Elliott, N. Gaaloul, E. Giese, W. Herr, J. R. Kelloff, J. M. Kohel, N. E. Lay, M. Meister, G. Müller, H. Müller, K. Oudhiri, L. Phillips, A. Pichery, E. M. Rasel, A. Roura, M. Sbroscia, W. P. Schleich, C. Schneider, C. Schubert, B. Sen, R. J. Thompson, and N. P. Bigelow, Pathfinder experiments with atom interferometry in the Cold Atom Lab onboard the International Space Station, *Nat. Commun.* **15**, 6414 (2024).
- [7] D. Schlippert, C. Meiners, R. Rengelink, C. Schubert, D. Tell, É. Wodey, K. Zipfel, W. Ertmer, and E. Rasel, Matter-Wave Interferometry for Inertial Sensing and Tests of Fundamental Physics, in *CPT and Lorentz Symmetry* (World Scientific, 2020) pp. 37–40.
- [8] L. Badurina, E. Bentine, D. Blas, K. Bongs, D. Bortoletto, T. Bowcock, K. Bridges, W. Bowden, O. Buchmueller, C. Burrage, J. Coleman, G. Elert, J. Ellis, C. Foot, V. Gibson, M. Haehnel, T. Harte, S. Hedges, R. Hobson, M. Holynski, *et al.*, AION: an atom interferometer observatory and network, *J. Cosmol. Astropart. Phys.* **2020** (05), 011.
- [9] L. Zhou, Z. Y. Xiong, W. Yang, B. Tang, W. C. Peng, K. Hao, R. B. Li, M. Liu, J. Wang, and M. S. Zhan, Development of an atom gravimeter and status of the 10-meter atom interferometer for precision gravity measurement, *Gen. Relativ. Gravitation* **43**, 1931 (2011).
- [10] T. Kovachy, P. Asenbaum, C. Overstreet, C. A. Donnelly, S. M. Dickerson, A. Sugarbaker, J. M. Hogan, and M. A. Kasevich, Quantum superposition at the half-metre scale, *Nature* **528**, 530 (2015).
- [11] F. Impens and C. J. Bordé, Space-time sensors using multiple-wave atom levitation, *Phys. Rev. A* **80**, 031602 (2009).
- [12] C. Schubert, S. Abend, M. Gersemann, M. Gebbe, D. Schlippert, P. Berg, and E. M. Rasel, Multi-loop atomic Sagnac interferometry, *Sci. Rep.* **11**, 16121 (2021).
- [13] C. Schubert, D. Schlippert, M. Gersemann, S. Abend, E. Giese, *et al.*, A scalable, symmetric atom interferometer for infrasound gravitational wave detection, *AVS Quantum Sci.* **6**, 044404 (2024).
- [14] S. Abend, M. Gebbe, M. Gersemann, H. Ahlers, H. Müntinga, E. Giese, N. Gaaloul, C. Schubert, C. Lämmerzahl, W. Ertmer, W. P. Schleich, and E. M. Rasel, Atom-Chip Fountain Gravimeter, *Phys. Rev. Lett.* **117**, 203003 (2016).
- [15] K. J. Hughes, J. H. T. Burke, and C. A. Sackett, Suspension of Atoms Using Optical Pulses, and Application to Gravimetry, *Phys. Rev. Lett.* **102**, 150403 (2009).
- [16] L. Morel, Z. Yao, P. Cladé, and S. Guellati-Khélifa, Determination of the fine-structure constant with an accuracy of 81 parts per trillion, *Nature* **588**, 61 (2020).
- [17] R. H. Parker, C. Yu, W. Zhong, B. Estey, and H. Müller, Measurement of the fine-structure constant as a test of the Standard Model, *Science* **360**, 191 (2018).
- [18] P. Asenbaum, C. Overstreet, M. Kim, J. Curti, and M. A. Kasevich, Atom-Interferometric Test of the Equivalence Principle at the 10^{-12} Level, *Phys. Rev. Lett.* **125**, 191101 (2020).
- [19] M. Gebbe, J.-N. Siemß, M. Gersemann, H. Müntinga, S. Herrmann, C. Lämmerzahl, H. Ahlers, N. Gaaloul, C. Schubert, K. Hammerer, S. Abend, and E. M. Rasel, Twin-lattice atom interferometry, *Nat. Commun.* **12**, 2544 (2021).
- [20] B. Canuel, S. Abend, P. Amaro-Seoane, F. Badaracco, Q. Beaufils, A. Bertoldi, K. Bongs, P. Bouyer, C. Braxmaier, W. Chaibi, N. Christensen, F. Fitzek, G. Flouris, N. Gaaloul, S. Gaffet, C. L. Garrido Alzar, R. Geiger, S. Guellati-Khelifa, K. Hammerer, J. Harms, *et al.*, ELGAR—a European Laboratory for Gravitation and Atom-interferometric Research, *Classical Quantum Gravity* **37**, 225017 (2020).
- [21] M.-S. Zhan, J. Wang, W.-T. Ni, D.-F. Gao, G. Wang, L.-X. He, R.-B. Li, L. Zhou, X. Chen, J.-Q. Zhong, B. Tang, Z.-W. Yao, L. Zhu, Z.-Y. Xiong, S.-B. Lu, G.-H. Yu, Q.-F. Cheng, M. Liu, Y.-R. Liang, P. Xu, *et al.*, ZAIGA: Zhaoshan long-baseline atom interferometer gravitation antenna, *Int. J. Mod. Phys. D* **29**, 1940005 (2020).
- [22] S. Abend, B. Allard, I. Alonso, J. Antoniadis, H. Araújo, G. Arduini, A. S. Arnold, T. Asano, N. Augst, L. Badurina, A. Balaž, H. Banks, M. Barone, M. Barsanti, A. Bassi, B. Battelier, C. F. A. Baynham, Q. Beaufils, A. Belić, A. Beniwal, *et al.*, Terrestrial very-long-baseline atom interferometry: Workshop summary, *AVS Quantum Sci.* **6**, 024701 (2024).
- [23] M. Abe, P. Adamson, M. Borcean, D. Bortoletto, K. Bridges,

- S. P. Carman, S. Chattopadhyay, J. Coleman, N. M. Curfman, K. DeRose, T. Deshpande, S. Dimopoulos, C. J. Foot, J. C. Frisch, B. E. Garber, S. Geer, V. Gibson, J. Glick, P. W. Graham, S. R. Hahn, *et al.*, Matter-wave Atomic Gradiometer Interferometric Sensor (MAGIS-100), *Quantum Sci. Technol.* **6**, 044003 (2021).
- [24] P. Cladé, S. Guellati-Khélifa, F. Nez, and F. Biraben, Large Momentum Beam Splitter Using Bloch Oscillations, *Phys. Rev. Lett.* **102**, 240402 (2009).
- [25] G. D. McDonald, C. C. N. Kuhn, S. Bennetts, J. E. Debs, K. S. Hardman, M. Johnsson, J. D. Close, and N. P. Robins, $80\hbar k$ momentum separation with Bloch oscillations in an optically guided atom interferometer, *Phys. Rev. A* **88**, 053620 (2013).
- [26] Z. Pagel, W. Zhong, R. H. Parker, C. T. Olund, N. Y. Yao, *et al.*, Symmetric Bloch oscillations of matter waves, *Phys. Rev. A* **102**, 053312 (2020).
- [27] T. Rahman, A. Wirth-Singh, A. Ivanov, D. Gochnauer, E. Hough, *et al.*, Bloch oscillation phases investigated by multipath Stückelberg atom interferometry, *Phys. Rev. Res.* **6**, L022012 (2024).
- [28] F. Fitzek, J.-N. Kirsten-Siemß, E. M. Rasel, N. Gaaloul, and K. Hammerer, Accurate and efficient Bloch-oscillation-enhanced atom interferometry, *Phys. Rev. Res.* **6**, L032028 (2024).
- [29] J. Rudolph, T. Wilkason, M. Nantel, H. Swan, C. M. Holland, *et al.*, Large Momentum Transfer Clock Atom Interferometry on the 689 nm Intercombination Line of Strontium, *Phys. Rev. Lett.* **124**, 083604 (2020).
- [30] P. Berg, S. Abend, G. Tackmann, C. Schubert, E. Giese, *et al.*, Composite-Light-Pulse Technique for High-Precision Atom Interferometry, *Phys. Rev. Lett.* **114**, 063002 (2015).
- [31] J. M. McGuirk, M. J. Snadden, and M. A. Kasevich, Large Area Light-Pulse Atom Interferometry, *Phys. Rev. Lett.* **85**, 4498 (2000).
- [32] T. Lévêque, A. Gauguier, F. Michaud, F. Pereira Dos Santos, and A. Landragin, Enhancing the Area of a Raman Atom Interferometer Using a Versatile Double-Diffraction Technique, *Phys. Rev. Lett.* **103**, 080405 (2009).
- [33] E. Giese, A. Roura, G. Tackmann, E. M. Rasel, and W. P. Schleich, Double Bragg diffraction: A tool for atom optics, *Phys. Rev. A* **88**, 053608 (2013).
- [34] J. Küber, F. Schmaltz, and G. Birkl, *Experimental realization of double Bragg diffraction: robust beamsplitters, mirrors, and interferometers for Bose-Einstein condensates* (2016), arXiv:1603.08826 [cond-mat.quant-gas].
- [35] S. Hartmann, J. Jenewein, E. Giese, S. Abend, A. Roura, *et al.*, Regimes of atomic diffraction: Raman versus Bragg diffraction in retroreflective geometries, *Phys. Rev. A* **101**, 053610 (2020).
- [36] S. Hartmann, J. Jenewein, S. Abend, A. Roura, and E. Giese, Atomic Raman scattering: Third-order diffraction in a double geometry, *Phys. Rev. A* **102**, 063326 (2020).
- [37] H. Müller, S.-w. Chiow, Q. Long, S. Herrmann, and S. Chu, Atom Interferometry with up to 24-Photon-Momentum-Transfer Beam Splitters, *Phys. Rev. Lett.* **100**, 180405 (2008).
- [38] H. Ahlers, H. Müntinga, A. Wenzlawski, M. Krutzik, G. Tackmann, S. Abend, N. Gaaloul, E. Giese, A. Roura, R. Kuhl, C. Lämmerzahl, A. Peters, P. Windpassinger, K. Sengstock, W. P. Schleich, W. Ertmer, and E. M. Rasel, Double Bragg Interferometry, *Phys. Rev. Lett.* **116**, 173601 (2016).
- [39] H. Müller, S.-w. Chiow, S. Herrmann, and S. Chu, Atom Interferometers with Scalable Enclosed Area, *Phys. Rev. Lett.* **102**, 240403 (2009).
- [40] M. Chiarotti, J. N. Tinsley, S. Bandarupally, S. Manzoor, M. Sacco, *et al.*, Practical Limits for Large-Momentum-Transfer Clock Atom Interferometers, *PRX Quantum* **3**, 030348 (2022).
- [41] M. Büchner, R. Delhuille, A. Miffre, C. Robilliard, J. Vigué, *et al.*, Diffraction phases in atom interferometers, *Phys. Rev. A* **68**, 013607 (2003).
- [42] B. Estey, C. Yu, H. Müller, P.-C. Kuan, and S.-Y. Lan, High-Resolution Atom Interferometers with Suppressed Diffraction Phases, *Phys. Rev. Lett.* **115**, 083002 (2015).
- [43] A. Béguin, T. Rodzinka, J. Vigué, B. Allard, and A. Gauguier, Characterization of an atom interferometer in the quasi-Bragg regime, *Phys. Rev. A* **105**, 033302 (2022).
- [44] P. A. Altin, M. T. Johnsson, V. Negnevitsky, G. R. Dennis, R. P. Anderson, J. E. Debs, S. S. Szigeti, K. S. Hardman, S. Bennetts, G. D. McDonald, L. D. Turner, J. D. Close, and N. P. Robins, Precision atomic gravimeter based on Bragg diffraction, *New J. Phys.* **15**, 023009 (2013).
- [45] R. H. Parker, C. Yu, B. Estey, W. Zhong, E. Huang, and H. Müller, Controlling the multiport nature of Bragg diffraction in atom interferometry, *Phys. Rev. A* **94**, 053618 (2016).
- [46] J. Jenewein, S. Hartmann, A. Roura, and E. Giese, Bragg-diffraction-induced imperfections of the signal in retroreflective atom interferometers, *Phys. Rev. A* **105**, 063316 (2022).
- [47] T. Wilkason, M. Nantel, J. Rudolph, Y. Jiang, B. E. Garber, *et al.*, Atom Interferometry with Floquet Atom Optics, *Phys. Rev. Lett.* **129**, 183202 (2022).
- [48] T. Rodzinka, E. Dionis, L. Calmels, S. Beldjoudi, A. Béguin, D. Guéry-Odelin, B. Allard, D. Sugny, and A. Gauguier, Optimal Floquet state engineering for large scale atom interferometers, *Nat. Commun.* **15**, 10281 (2024).
- [49] Z. Chen, G. Louie, Y. Wang, T. Deshpande, and T. Kovachy, Enhancing strontium clock atom interferometry using quantum optimal control, *Phys. Rev. A* **107**, 063302 (2023).
- [50] J. Saywell, M. Carey, M. Belal, I. Kuprov, and T. Freegarde, Optimal control of Raman pulse sequences for atom interferometry, *J. Phys. B: At., Mol. Opt. Phys.* **53**, 085006 (2020).
- [51] J. Saywell, M. Carey, I. Kuprov, and T. Freegarde, Biselective pulses for large-area atom interferometry, *Phys. Rev. A* **101**, 063625 (2020).
- [52] R. Li, V. J. Martínez-Lahuerta, S. Seckmeyer, K. Hammerer, and N. Gaaloul, Robust double Bragg diffraction via detuning control, *Phys. Rev. Res.* **6**, 043236 (2024).
- [53] G. Louie, Z. Chen, T. Deshpande, and T. Kovachy, Robust atom optics for Bragg atom interferometry, *New J. Phys.* **25**, 083017 (2023).
- [54] J. C. Saywell, M. S. Carey, P. S. Light, S. S. Szigeti, A. R. Milne, K. S. Gill, M. L. Goh, V. S. Perunicic, N. M. Wilson, C. D. Macrae, A. Rischka, P. J. Everitt, N. P. Robins, R. P. Anderson, M. R. Hush, and M. J. Biercuk, Enhancing the sensitivity of atom-interferometric inertial sensors using robust control, *Nat. Commun.* **14**, 7626 (2023).
- [55] Y. Wang, J. Glick, T. Deshpande, K. DeRose, S. Saraf, N. Sachdeva, K. Jiang, Z. Chen, and T. Kovachy, Robust quantum control via multipath interference for thousandfold phase amplification in a resonant atom interferometer, *Phys. Rev. Lett.* **133**, 243403 (2024).
- [56] A. Béguin, T. Rodzinka, L. Calmels, B. Allard, and A. Gauguier, Atom Interferometry with Coherent Enhancement of Bragg Pulse Sequences, *Phys. Rev. Lett.* **131**, 143401 (2023).
- [57] J.-N. Kirsten-Siemß, F. Fitzek, C. Schubert, E. M. Rasel, N. Gaaloul, and K. Hammerer, Large-Momentum-Transfer Atom Interferometers with μrad -Accuracy Using Bragg Diffraction, *Phys. Rev. Lett.* **131**, 033602 (2023).
- [58] J.-N. Kirsten-Siemß, Theory of Large-Momentum-Transfer Atom Interferometry in the Quasi-Bragg Regime, *Ph.D. thesis*, Leibniz University Hannover, Hannover (2023).
- [59] J.-N. Siemß, F. Fitzek, S. Abend, E. M. Rasel, N. Gaaloul, *et al.*, Analytic theory for Bragg atom interferometry based on the adiabatic theorem, *Phys. Rev. A* **102**, 033709 (2020).

- [60] E. Giese, Mechanisms of matter-wave diffraction and their application to interferometers, *Fortschr. Phys.* **63**, 337 (2015).
- [61] B. Shore, *The Theory of Coherent Atomic Excitation, Multilevel Atoms and Incoherence*, A Wiley-Interscience publication (Wiley, New York, 1990).
- [62] T. Lauber, J. Küber, O. Wille, and G. Birkl, Optimized Bose-Einstein-condensate production in a dipole trap based on a 1070-nm multifrequency laser: Influence of enhanced two-body loss on the evaporation process, *Phys. Rev. A* **84**, 043641 (2011).
- [63] H. Müller, S.-w. Chiow, and S. Chu, Atom-wave diffraction between the Raman-Nath and the Bragg regime: Effective Rabi frequency, losses, and phase shifts, *Phys. Rev. A* **77**, 023609 (2008).
- [64] B. Plotkin-Swing, D. Gochnauer, K. E. McAlpine, E. S. Cooper, A. O. Jamison, *et al.*, Three-Path Atom Interferometry with Large Momentum Separation, *Phys. Rev. Lett.* **121**, 133201 (2018).
- [65] We use $\Omega_R = 0.42 \times 4P\tilde{U}_0(\lambda)/(\hbar\pi w_0^2)$, where P , w_0 , and $\lambda = 780.226$ nm are average power, waist, and wavelength of the Bragg beams. $\tilde{U}_0(\lambda)$ is the dipole factor [71–74] for ^{87}Rb . The factor 0.42 arises from $f(t)$. This definition has been verified by finding good agreement of Ω_R experimentally observed for resonant first-order diffraction and the one extracted from simulations.
- [66] S. S. Szigeti, J. E. Debs, J. J. Hope, N. P. Robins, and J. D. Close, Why momentum width matters for atom interferometry with Bragg pulses, *New J. Phys.* **14**, 023009 (2012).
- [67] W. Auzinger, H. Hofstätter, D. Ketcheson, and O. Koch, Practical splitting methods for the adaptive integration of nonlinear evolution equations. Part I: Construction of optimized schemes and pairs of schemes, *BIT Numer. Math.* **57**, 55 (2017).
- [68] L. A. Sidorenkov, R. Gautier, M. Altorio, R. Geiger, and A. Landragin, Tailoring Multiloop Atom Interferometers with Adjustable Momentum Transfer, *Phys. Rev. Lett.* **125**, 213201 (2020).
- [69] L.-Y. Chih and M. Holland, Reinforcement-learning-based matter-wave interferometer in a shaken optical lattice, *Phys. Rev. Res.* **3**, 033279 (2021).
- [70] L. Hu, N. Poli, L. Salvi, and G. M. Tino, Atom Interferometry with the Sr Optical Clock Transition, *Phys. Rev. Lett.* **119**, 263601 (2017).
- [71] J. Küber, Dynamics of Bose-Einstein condensates in novel optical potentials, *Ph.D. thesis*, Technische Universität Darmstadt, Darmstadt (2014).
- [72] H. J. Metcalf and P. Van der Straten, *Laser cooling and trapping* (Springer Science & Business Media, New York, 1999).
- [73] R. Grimm, M. Weidemüller, and Y. B. Ovchinnikov, Optical dipole traps for neutral atoms, in *Advances in atomic, molecular, and optical physics*, Vol. 42 (Elsevier, New York, 2000) pp. 95–170.
- [74] D. A. Steck, *Quantum and Atom Optics* (2024), revision 0.16.1.